Localized anisotropy in the mantle transition zone due to flow through slab gaps

Han Zhang[1], Brandon Schmandt[1], and Jin S Zhang[1]

[1]University of New Mexico

January 31, 2021

Abstract

Measurement of anisotropy advances our understanding of mantle dynamics by linking remote seismic observations to local deformation state through constraints from mineral physics. The Pacific Northwest records the largest depth-integrated anisotropic signals across the western United States but the depths contributing to the total signal are unclear. We used the amplitudes of orthogonally polarized P-to-S converted phases from the mantle transition zone boundaries to identify anisotropy within the ~400-700 km deep layer. Significant anisotropy is found near slab gaps. Focusing of mantle flow through slab gaps may lead to locally elevated stress that enhances lattice preferred orientation of anisotropic minerals within the transition zone, such as wadsleyite.

Title: Localized anisotropy in the mantle transition zone due to flow through slab gaps

Authors: Han Zhang[1*], Brandon Schmandt[1], Jin S. Zhang[1,2]

Affiliations:

1. Department of Earth and Planetary Science, University of New Mexico, Albuquerque, NM, USA.
2. Institute of Meteoritics, University of New Mexico, Albuquerque, NM, USA.

*Correspondence to: hanzhang@unm.edu

Key Points:

- P_{SH}/P_{SV} amplitude ratios between *P*660*s* and *P*410*s* are useful for constraining transition zone anisotropy
- Evidence for up to 2% mantle transition zone anisotropy is found beneath the Pacific Northwest of the U.S.
- Mantle flow between slab fragments may enhance development of transition zone anisotropy

Abstract:

Measurement of anisotropy advances our understanding of mantle dynamics by linking remote seismic observations to local deformation state through constraints from mineral physics. The Pacific Northwest records the largest depth-integrated anisotropic signals across the western United States but the depths contributing to the total signal are unclear. We used the amplitudes of orthogonally polarized P-to-S converted phases from the mantle transition zone boundaries to identify anisotropy within the ~400-700 km deep layer. Significant anisotropy is found near slab gaps imaged by prior tomography. Focusing of mantle flow through slab gaps may lead to locally elevated stress that enhances lattice preferred orientation of anisotropic minerals within the transition zone, such as wadsleyite.

Plain Language Summary:

Earth's mantle convects like a fluid over geological time and it organizes mineral fabrics resulting in directional dependence of seismic velocities, i.e. seismic anisotropy. There is abundant evidence for flow-induced seismic anisotropy at depths above about 400 km, but it is less clear if anisotropy is developed in the mantle transition zone at about 400-700 km deep. Here, we use seismic waves generated from the bottom and top of the transition zone to constrain anisotropy within the layer. Localized evidence of strong anisotropy is found beneath the Pacific Northwest near locations where prior imaging studies show gaps between subducted oceanic plate fragments. We propose that focused flow through constrictions like slab gaps may cause seismic anisotropy in the mantle transition zone.

Introduction

Seismic anisotropy of Earth's mantle provides important insights into convective flow and composition at inaccessible depths. There is abundant evidence for concentrated anisotropy at depths within a few hundred kilometers of the mantle's top and bottom, but the prevalence of anisotropy at intermediate depths is more uncertain (Long & Becker, 2010). Potential reasons for diminished anisotropy in the transition zone and most of the lower mantle include decreasing anisotropy of higher-pressure olivine polymorphs (Mainprice 2015; Zhang et al., 2018), strain partitioning into localized shear zones (Girard et al., 2016), and accommodation of strain by diffusion creep rather than dislocation creep (Mohiuddin et al., 2020; Ritterbex et al., 2020). Depth-integrated measurements of mantle anisotropy like teleseismic shear wave splitting (SWS) are often assumed to be dominated by anisotropy at depths less than ~300 km. This perspective is supported by the positive correlation of fast-axis orientations with plate tectonic deformation and surface wave azimuthal anisotropy (Becker et al., 2012; Long & Becker, 2010), as well as isolated evidence that local deep earthquakes exhibit SWS comparable to teleseismic measurements (Fischer & Wiens, 1996). However, some long-wavelength global imaging studies and regional attempts to separate near-source contributions to path-integrated SWS suggest anisotropy extending to mantle transition zone depths of about 400-700 km (Huang et al., 2019; Lynner & Long, 2015; Yuan & Beghein, 2013).

The Pacific Northwest (PNW) of the U.S. is well-suited to investigate the depth distribution of mantle anisotropy (Fig. 1a). Active subduction is thought to organize vigorous mantle flow, the region has been densely instrumented with broadband seismometers, and a large depth-integrated anisotropy signal is indicated by spatially averaged teleseismic SWS measurements (Liu et al., 2014; Long et al., 2012; Supporting Information S1) (Fig. 1c). Surface wave azimuthal anisotropy constrains regional anisotropy at depths less than about 200 km, but that depth interval can only account for about half of the anisotropy indicated by SWS (Wagner & Long, 2013). Recent attempts using finite-frequency *SKS* splitting intensity suggest up to 8% anisotropy at 200-400 km to accommodate the remaining signal (Mondal & Long, 2020). However, the amplitude of the sensitivity kernels reduces with depth, leaving uncertainty about anisotropy at >400 km depth. Recent full-waveform inversion (FWI) for anisotropic velocities using regional earthquakes suggests that subduction-driven flow beneath the PNW creates anisotropy at transition zone depths (Zhu et al., 2020). The fast orientations from FWI tomography generally agree with SWS, but the depth-integrated magnitude of anisotropy is much smaller than that obtained by SWS. Thus, it is unclear how much transition zone anisotropy is needed to explain the large depth-integrated SWS signals in the PNW.

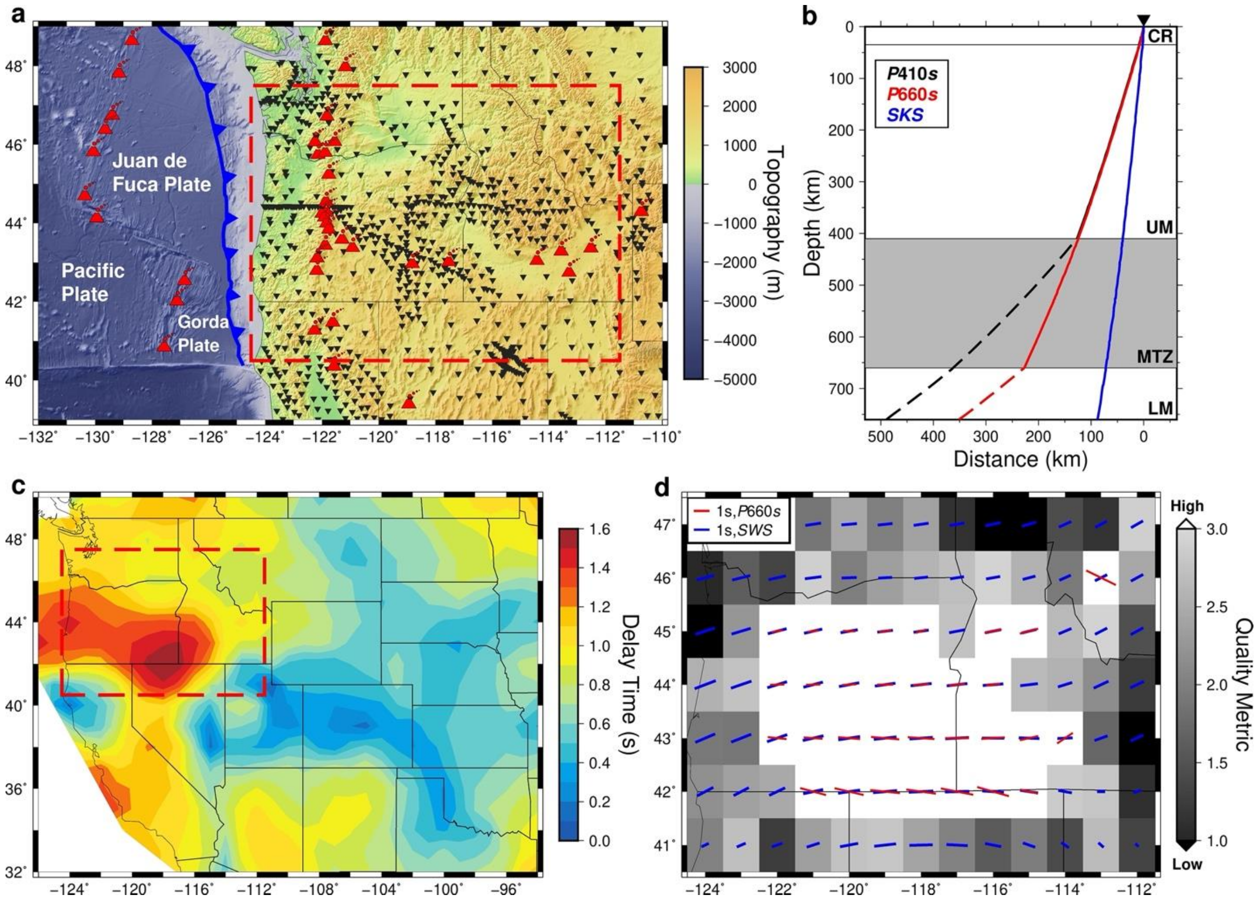

Fig. 1. Tectonic setting of the PNW and seismic observations of anisotropy. (**a**) The Juan de Fuca Plate is actively subducting beneath the PNW. Holocene volcanoes (red symbols) and broadband seismometers (black inverse triangles) are superimposed on the topography. The red dashed box outlines our study area. (**b**) Ray paths of the *P*410*s* (black), *P*660*s* (red) and *SKS* (blue) phases. Compositional layers are labeled: crust (CR), upper mantle (UM), mantle transition zone (MTZ), and lower mantle (LM). (**c**) Spatially averaged SWS delay times in the western U.S. The red dashed box outlines our study region. (**d**) Comparison between our estimated splitting parameters from the *P*660*s* (red bar) and the spatially averaged SWS results (blue bar). The grayscale background indicates the quality of the estimations from the *P*660*s*.

Data and Method

This study takes advantage of teleseismic P-to-S (*Ps*) conversions at the boundaries of the mantle transition zone to isolate potential deep contributions to anisotropy beneath the PNW. The two converted phases, *P*410*s* and *P*660*s*, almost share ray paths in the upper mantle so the paired observations can localize signals from within the transition zone (Fig. 1b). In an isotropic mantle with 1-D velocity structure, *Ps* conversions would only be observed with P-SV polarization. But constructive anisotropy along the shear wave ray path can cause splitting effect, leading to observations of *Ps* energy on SH polarization. We collected broadband waveform data from teleseismic earthquakes with magnitude greater than 5.5. For data with P wave signal-to-noise ratio (SNR) greater than 3, we extracted 3-component (P-SV-SH) receiver functions using a multimode frequency domain deconvolution method (Mercier et al., 2006). The receiver functions were filtered using a zero-phase bandpass filter between 0.07 Hz and 0.25 Hz and corrected for normal moveout by extracting velocities along the ray paths within a previous tomographic model (Schmandt & Lin, 2014).

Since small delay times often yield undetectable *Ps* signal on the SH component (Montagner et al., 2000), stacking many waveforms is often required and attempts to use the two phases are limited to areas with strong anisotropy (Vinnik & Montagner, 1996; Kong et al., 2018). Based on their piercing points at 500 km depth, we stacked the receiver functions that sample the transition zone in 200 km radius caps. We then applied a bootstrap based quality metric to determine regions with adequate SNR to constrain transition zone anisotropy (Fig. 1d; Supporting Information S2). The region with adequate *P*660*s* signals corresponds well with the area of large SWS delay times (>1.3 s, Fig. 1c). The splitting parameters, fast-axis orientation and delay time, estimated from *P*660*s* using transverse energy minimization (Long & Silver, 2009; Walsh et al., 2013) also share great similarity with the SWS results, indicating that most of the anisotropic signals can be explained at depths above the 660 (Fig. 1d). The mean difference of the fast-axis orientation estimates is 6.1° with a standard deviation of 11.8°, and the mean difference of delay times is -0.03 s with a standard deviation of 0.34 s. However, the transverse component energy minimization approach to measuring anisotropy results in large delay time uncertainties (~0.5 s) for the *P*410*s* and

*P*660*s* estimations at individual stacking points, so they are not optimal for constraining the potentially weak anisotropy in the transition zone.

The amplitude ratio of the conversions between the two shear wave components (P_{SH}/P_{SV}) provides greater sensitivity to the magnitude of anisotropy than the delay time (Fig. S1). Consequently, the differences in the P_{SH}/P_{SV} amplitude ratios between *P*660*s* and *P*410*s* reflect transition zone anisotropy more precisely. Pairing the two *Ps* phases during the measurement further eliminates the back-azimuth component from the anisotropic effects. We again measured the amplitude ratios using stacks in 200 km radius caps and applied bootstrap resampling to assess the uncertainty (Supporting Information S3). The measurement of amplitude ratios of receiver functions is similar to the conventional method of measuring splitting intensity for the *SKS* phase (Chevrot, 2000). The splitting intensity is defined as the amplitude ratio of the *SKS* phase between the transverse component and the time derivative of the radial component. In contrast, we measured the amplitude ratio of the stacked *Ps* phase between the time integrated SH component (P_{SH}) and original SV component (P_{SV}). Mathematically, the derivative and integration processes offer identical results after removing the integration constant. The integration process we adopted here preserves the one-side polarity of the P_{SV} phase, which simplifies the measurements (Fig. S1).

Results and Discussion

The null hypothesis of an isotropic transition zone and all anisotropy above the 410 predicts indistinguishable amplitude ratio distributions for the two phases. We use Cohen's distance between the *P*660*s* and *P*410*s* amplitude ratio distributions and the corresponding paired t-test to evaluate the significance of transition zone anisotropy (Supporting Information S3). About half of the resulting Cohen's distances show a significant difference at 68% confidence (±1.0), with a few locations exceeding the 95% confidence level (±2.0) (Fig. 2, b and d, See Fig. S2 for more examples).

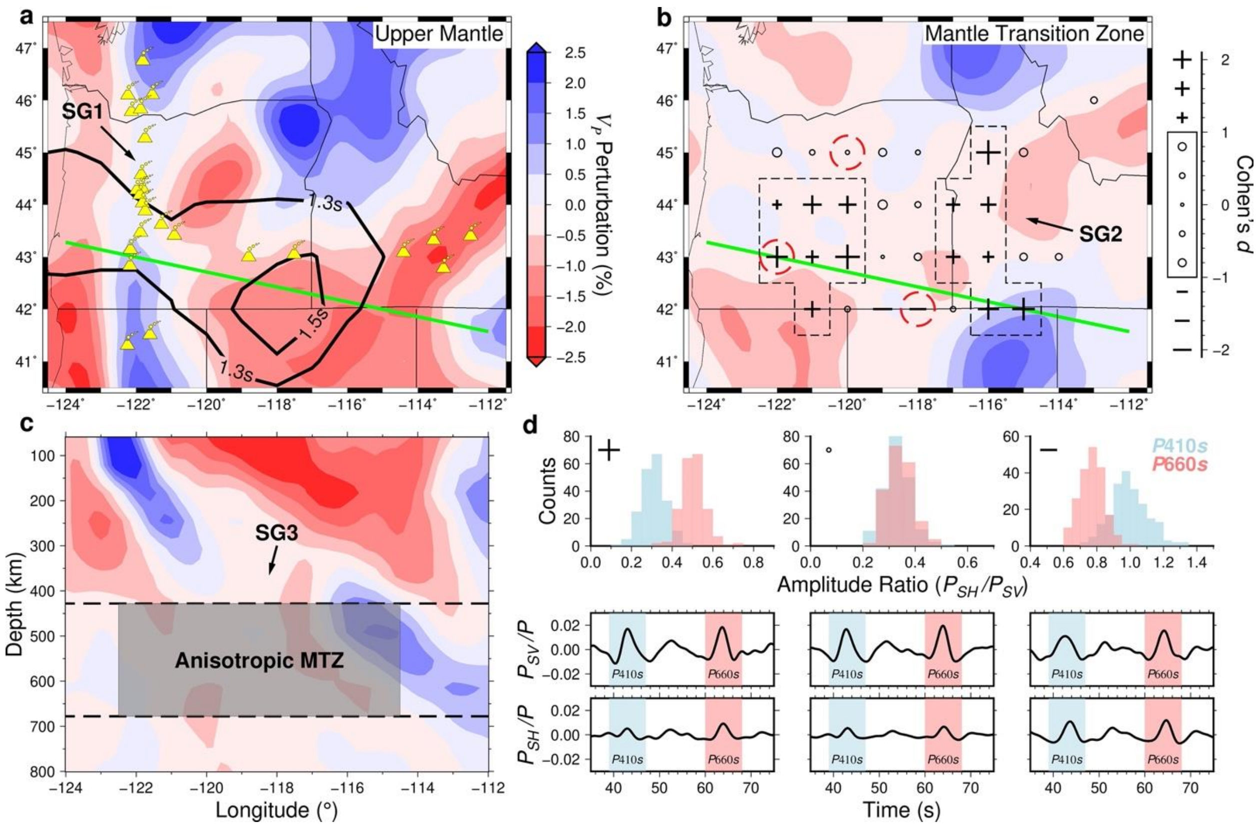

Fig. 2. Seismic tomography of the study region and amplitude ratio evidence for anisotropy. Depth averaged V_P perturbation within (**a**) the upper mantle (60-350 km) and (**b**) the mantle transition zone (435-635 km). The positions of slab gaps are labeled by SG. Holocene volcanoes (yellow symbols), contoured spatially averaged SWS delay times (1.3s and 1.5s, black lines), and observed Cohen's distances are superimposed on the tomography. (**c**) Cross section of the V_P perturbation beneath the green line on the maps. The gray box outlines where mantle transition zone (MTZ) anisotropy is required by the observations. (**d**) Examples of the observed amplitude ratios and stacked waveforms from the locations with red dashed circles in panel b. The amplitude ratios from the *P*410*s* are in red while those from *P*660*s* are in blue.

We defined three categories for the observed results: constructive interference where *P*660*s* amplitude ratios are greater than *P*410*s* amplitude ratios (labeled '+'), destructive interference where *P*410*s* amplitude ratios are greater than those of *P*660*s* (labeled '-'), and neutral where there is no significant difference (labeled '○'; Fig. 2b). The neutral observations fail to reject the null hypothesis of an isotropic transition zone. Two larger areas of constructive interference and one smaller area of destructive interference indicate localized transition zone anisotropy inboard of the Cascades volcanic arc (Fig. 2c).

The two constructive interference areas exhibit greater path-integrated anisotropy from the 660 to the surface compared to that from the 410 to the surface. Such observations can be fit with a common fast orientation for an anisotropic layer extending through the upper mantle and into the transition zone. Both constructive interference areas lie within gaps between high-velocity slab fragments identified by seismic tomography (Schmandt & Lin, 2014; Hawley & Allen, 2019) (Fig. 2, a and b, labeled SG; see Movie S1 for 3D illustration). The western area is located near an along-strike slab gap in the upper mantle beneath the central to southern Oregon backarc region that is hypothesized to focus mantle flow beneath backarc volcanic provinces (Hawley & Allen, 2019). The eastern area of constructive interference is located between two high-velocity features interpreted to be older slab fragments located further beneath the continental interior (Liu & Stegman, 2011; Schmandt & Humphreys, 2011). The southern edge of the eastern constructive interference area appears to overlap the position of the high-velocity slab beneath northern Nevada.

Two stacking points that exhibit destructive interference of transition zone and upper mantle anisotropy are located at the southern edge of the well-resolved area (Fig. 2b). Deconstructive interference of splitting within the transition zone and above it due to changing fast orientation with depth can create a larger P_{SH}/P_{SV} amplitude ratio of the *P*410*s* compared to that of *P*660*s* (Fig. S3; Supporting Information S4). Given the small area that exhibits destructive interference and the tradeoffs among estimating the thickness, fast orientation, and magnitude of anisotropy for the two layers, we refrain from further interpretation of these two stacking points.

Anisotropy within the transition zone could arise on account of lattice preferred orientation (LPO) of olivine polymorphs. Wadsleyite is the stable polymorph of olivine in the upper transition zone and has a maximum single-crystal shear wave anisotropy of ~9% (Zhang et al., 2018). The peak anisotropy is smaller than that of olivine above the 410 (Fig. S4), but deformation experiments have successfully produced up to 2% anisotropy of wadsleyite (Kawazoe et al., 2013; Ohuchi et al., 2014). At lower transition zone depths, the stable polymorph of olivine is ringwoodite and it is elastically almost isotropic at transition zone pressures (Mainprice, 2015). Therefore, it is unlikely to contribute to the observed anisotropic signals. Atypical anisotropic minerals formed near or within the subducted slab may contribute to anisotropy. At relatively low mantle temperatures, two strongly anisotropic minerals, phase E and akimotoite, could form at transition zone depths (Hao et al., 2019; Satta et al., 2019). Phase E is a reaction product between olivine and water at upper transition zone depths (Satta et al., 2019). Akimotoite is enriched in the refractory harzburgitic lithosphere of the slabs at lower transition zone depths (Ishii et al., 2019). Both minerals have single-crystal shear wave anisotropy up to ~20%, which makes them alternative candidates for the origin of observed anisotropic signals in the transition zone.

The deformation mechanisms for the mantle transition zone minerals depend on many factors, such as temperature, flow stress, strain rates, and grain size. The laboratory determined glide-driven dislocation creep of transition zone minerals can cause development of LPO (Kawazoe et al., 2013). However, a recent theoretical study suggests that deformation in the mantle transition zone is dominated by climb-driven dislocation creep, which does not develop LPO (Ritterbex et al., 2020). The glide-driven dislocation creep is favored by high stress and strain rates in the laboratory, whereas typical flow stress and strain rates in the ambient mantle are several orders lower. Therefore, the development of LPO may be expected only in areas of stress concentration, such as where mantle flow is focused through constrictions (Alisic et al., 2012; Király et al., 2020).

Based on the mineral physics' constraints, we constructed three types of forward models to illustrate a range of potential anisotropic structures (Fig. 3a; Supporting Information S5). The simplest model includes only upper mantle anisotropy extending from the Moho to 400 km depth, such that anisotropy is consistent with only an olivine LPO origin (Fig. 3a, #1). Since there is no anisotropy within the transition zone, the first model can explain the neutral observations where the P_{SH}/P_{SV} amplitude ratios from the $P660s$ and $P410s$ are indistinguishable.

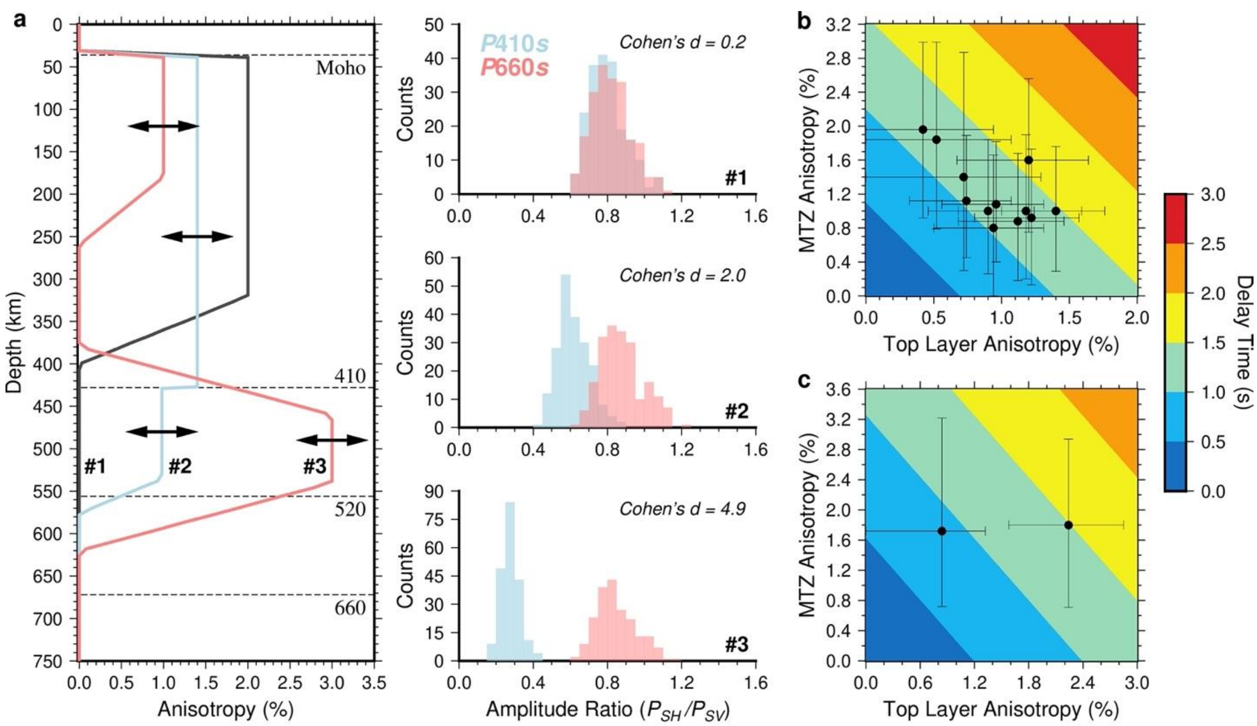

Fig. 3. Forward models and the inverted mantle transition zone anisotropy. (**a**) Three types of forward models (#1-3) and their corresponding amplitude ratios distributions. The Cohen's distances are denoted by the histograms. (**b**) Inverted mantle transition zone (MTZ) anisotropy for most of the constructive interference areas using parameterization of model #2. The error bar

represents the 68% confidence intervals. The color background represents the delay time from a vertically propagated shear wave. (**c**) Inverted results for the two stacking points in the southeastern corner using parameterization of model #3.

The second model also contains upper mantle anisotropy, but it is underlain by an anisotropic layer in the upper part of the transition zone where wadsleyite is stable (Fig. 3a, #2). This model yields constructive interference of transition zone and upper mantle splitting effect and then offers a plausible explanation for places with a larger *P*660*s* amplitude ratio. With this model parameterization, we used a grid search of upper mantle and transition zone anisotropy magnitudes to find the best model for explaining the observations (Supporting Information S6). Using a ray parameter and back-azimuth distribution identical to the observational data, the inverted results show that inclusion of ~1-2 % anisotropy in the upper mantle transition zone can reproduce the observed differences between the two amplitude ratios for most stacking points exhibiting constructive interference (Fig. 3b).

The third model is built on the idea that subducted slab is present in the transition zone, thus atypical minerals which are not expected in the ambient mantle may contribute to anisotropy (Fig. 3a, #3). In this case, the anisotropy within the transition zone is allowed to extend to deeper depths where wadsleyite is no longer stable. The deeper anisotropy may arise from akimotoite associated with the cool slab fragment, such as beneath the southeastern corner of the well-resolved area (Fig. 2b). When modeling the two stacking points in the southeastern corner, the additional thickness of the anisotropic layer prevents requiring unreasonably large anisotropy in the wadsleyite stability field (Fig. 3c).

The three anisotropic structures suggest various geodynamic settings (Fig. 4). The first model represents upper mantle flow due to absolute plate motion and subduction zone corner flow in the shallow upper mantle. In this conventional context, anisotropy is primarily due to olivine LPO created by flow-induced dislocation creep. The second model requires focused mantle flow caused by slab ruptures as hypothesized by prior geodynamic modeling of regional mantle flow and anisotropic fast orientations (Zhou et al., 2018). If flow through slab gaps induces locally high stress at transition zone depths, the LPO of wadsleyite could contribute a portion (up to 0.4 s in this study) of the total splitting delay time. The additional anisotropy at transition zone depths helps explain the large discrepancy between estimated splitting delay times from surface wave azimuthal anisotropy studies and observed teleseismic SWS in the central Cascades backarc (Wagner & Long, 2013). The third model represents the potential influence of compositional heterogeneity due to a slab fragment at transition zone depths, which is a scenario that may be even more important for subduction zones with older and colder slab fragments in the transition zone.

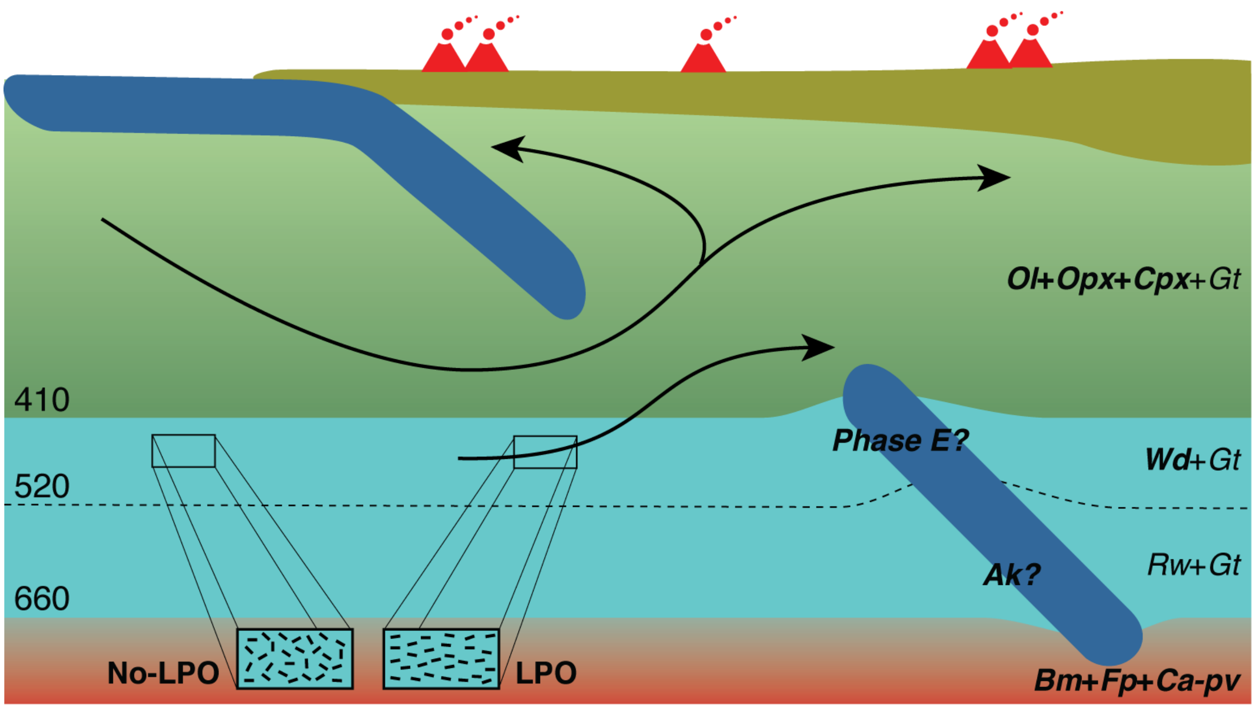

Fig. 4. Schematic model of flow going through slab gap. The rupture of a continuous slab induces enhanced flow near the slab gap. The resulting flow concentrates stress and develops lattice preferred orientation (LPO) of anisotropic minerals at transition zone depths. Common minerals are labeled using italic font with anisotropic minerals in bold: olivine (Ol),

orthopyroxene (Opx), clinopyroxene (Cpx), garnet (Gt), wadsleyite (Wd), ringwoodite (Rw), bridgmanite (Bm), ferropericlase (Fp), Ca-perovskite (Ca-pv), akimotoite (Ak).

Conclusions

The new results support the potential development of seismic anisotropy at mantle transition zone depths, with magnitudes that can be similar to those in the upper mantle. However, in contrast to upper mantle anisotropy that is observed ubiquitously, it appears that transition zone anisotropy may be restricted to areas of locally high stress such as focused flow through fragmented slabs.

References

1. Alisic, L., Gurnis, M., Stadler, G., Burstedde, C., & Ghattas, O. (2012). Multi-scale dynamics and rheology of mantle flow with plates. *Journal of Geophysical Research: Solid Earth*, *117*(B10).
2. Becker, T. W., Lebedev, S., & Long, M. D. (2012). On the relationship between azimuthal anisotropy from shear wave splitting and surface wave tomography. *Journal of Geophysical Research: Solid Earth*, *117*(B1).
3. Chevrot, S. (2000). Multichannel analysis of shear wave splitting. *Journal of Geophysical Research: Solid Earth*, *105*(B9), 21579-21590.
4. Fischer, K. M., & Wiens, D. A. (1996). The depth distribution of mantle anisotropy beneath the Tonga subduction zone. *Earth and Planetary Science Letters*, *142*(1-2), 253-260.
5. Girard, J., Amulele, G., Farla, R., Mohiuddin, A., & Karato, S. I. (2016). Shear deformation of bridgmanite and magnesiowüstite aggregates at lower mantle conditions. *Science*, *351*(6269), 144-147.
6. Hao, S., Wang, W., Qian, W., & Wu, Z. (2019). Elasticity of akimotoite under the mantle conditions: Implications for multiple discontinuities and seismic anisotropies at the depth of∼ 600–750 km in subduction zones. *Earth and Planetary Science Letters*, *528*, 115830.
7. Hawley, W. B., & Allen, R. M. (2019). The fragmented death of the Farallon plate. *Geophysical Research Letters*, *46*(13), 7386-7394.
8. Huang, Q., Schmerr, N., Waszek, L., & Beghein, C. (2019). Constraints on seismic anisotropy in the mantle transition zone from long-period SS precursors. *Journal of Geophysical Research: Solid Earth*, *124*(7), 6779-6800.
9. Ishii, T., Kojitani, H., & Akaogi, M. (2019). Phase Relations of Harzburgite and MORB up to the Uppermost Lower Mantle Conditions: Precise Comparison With Pyrolite by Multisample Cell High-Pressure Experiments With Implication to Dynamics of Subducted Slabs. *Journal of Geophysical Research: Solid Earth*, *124*(4), 3491-3507.

10. Kawazoe, T., Ohuchi, T., Nishihara, Y., Nishiyama, N., Fujino, K., & Irifune, T. (2013). Seismic anisotropy in the mantle transition zone induced by shear deformation of wadsleyite. *Physics of the Earth and Planetary Interiors*, *216*, 91-98.
11. Király, Á., Portner, D. E., Haynie, K. L., Chilson-Parks, B. H., Ghosh, T., Jadamec, M., et al., (2020). The effect of slab gaps on subduction dynamics and mantle upwelling. *Tectonophysics*, *785*, 228458.
12. Kong, F., Gao, S.S., Liu, K.H., Song, J., Ding, W., Fang, Y., Ruan, A., & Li, J. (2018). Receiver function investigations of seismic anisotropy layering beneath Southern California. *Journal of Geophysical Research: Solid Earth*, *123*(12), 10-672.
13. Liu, L., & Stegman, D. R. (2011). Segmentation of the Farallon slab. *Earth and Planetary Science Letters*, *311*(1-2), 1-10.
14. Liu, K.H., Elsheikh, A., Lemnifi, A., Purevsuren, U., Ray, M., Refayee, H., et al., (2014). A uniform database of teleseismic shear wave splitting measurements for the western and central United States. *Geochemistry, Geophysics, Geosystems*, *15*(5), 2075-2085.
15. Long, M. D., Becker, T. W. (2010). Mantle dynamics and seismic anisotropy. *Earth and Planetary Science Letters*, *297*(3-4), 341-354.
16. Long, M. D., & Silver, P. G. (2009). Shear wave splitting and mantle anisotropy: Measurements, interpretations, and new directions. *Surveys in Geophysics*, *30*(4), 407-461.
17. Long, M.D., Till, C.B., Druken, K.A., Carlson, R.W., Wagner, L.S., Fouch, M.J., et al., (2012). Mantle dynamics beneath the Pacific Northwest and the generation of voluminous back-arc volcanism. *Geochemistry, Geophysics, Geosystems*, *13*(8).
18. Lynner, C., & Long, M. D. (2015). Heterogeneous seismic anisotropy in the transition zone and uppermost lower mantle: evidence from South America, Izu-Bonin and Japan. *Geophysical Journal International*, *201*(3), 1545-1552.
19. Mainprice, D. (2015) Seismic anisotropy of the deep Earth from a mineral and rock physics perspective. *Treatise in Geophysics*, *2nd Edition*, *Volume 2*, 487-538
20. Mercier, J. P., Bostock, M. G., & Baig, A. M. (2006). Improved Green's functions for passive-source structural studies. *Geophysics*, *71*(4), SI95-SI102.
21. Mohiuddin, A., Karato, S. I., & Girard, J. (2020). Slab weakening during the olivine to ringwoodite transition in the mantle. *Nature Geoscience*, *13*(2), 170-174.
22. Mondal, P., & Long, M. D. (2020). Strong seismic anisotropy in the deep upper mantle beneath the Cascadia backarc: Constraints from probabilistic finite-frequency SKS splitting intensity tomography. *Earth and Planetary Science Letters*, *539*, 116172.
23. Montagner, J. P., Griot-Pommera, D. A., & Lavé, J. (2000). How to relate body wave and surface wave anisotropy?. *Journal of Geophysical Research: Solid Earth*, *105*(B8), 19015-19027.
24. Ohuchi, T., Fujino, K., Kawazoe, T., & Irifune, T. (2014). Crystallographic preferred orientation of wadsleyite and ringwoodite: Effects of phase transformation and water on seismic anisotropy in the mantle transition zone. *Earth and Planetary Science Letters*, *397*, 133-144.

25. Ritterbex, S., Carrez, P., & Cordier, P. (2020). Deformation across the mantle transition zone: A theoretical mineral physics view. *Earth and Planetary Science Letters*, *547*, 116438.
26. Satta, N., Marquardt, H., Kurnosov, A., Buchen, J., Kawazoe, T., McCammon, C., & Ballaran, T. B. (2019). Single-crystal elasticity of iron-bearing phase E and seismic detection of water in Earth's upper mantle. *American Mineralogist*, *104*(10), 1526-1529.
27. Schmandt, B., & Humphreys, E. (2011). Seismically imaged relict slab from the 55 Ma Siletzia accretion to the northwest United States. *Geology*, *39*(2), 175-178.
28. Schmandt, B., & Lin, F. C. (2014). P and S wave tomography of the mantle beneath the United States. *Geophysical Research Letters*, *41*(18), 6342-6349.
29. Vinnik, L., & Montagner, J. P. (1996). Shear wave splitting in the mantle Ps phases. *Geophysical Research Letters*, *23*(18), 2449-2452.
30. Wagner, L. S., & Long, M. D. (2013). Distinctive upper mantle anisotropy beneath the High Lava Plains and Eastern Snake River Plain, Pacific Northwest, USA. *Geochemistry, Geophysics, Geosystems*, *14*(10), 4647-4666
31. Walsh, E., Arnold, R., & Savage, M. K. (2013). Silver and Chan revisited. *Journal of Geophysical Research: Solid Earth*, *118*(10), 5500-5515.
32. Yuan, K., & Beghein, C. (2013). Seismic anisotropy changes across upper mantle phase transitions. *Earth and Planetary Science Letters*, *374*, 132-144
33. Zhang, J. S., Bass, J. D., & Schmandt, B. (2018). The elastic anisotropy change near the 410-km discontinuity: Predictions from single-crystal elasticity measurements of olivine and wadsleyite. *Journal of Geophysical Research: Solid Earth*, *123*(4), 2674-2684.
34. Zhou, Q., Hu, J., Liu, L., Chaparro, T., Stegman, D. R., & Faccenda, M. (2018). Western US seismic anisotropy revealing complex mantle dynamics. *Earth and Planetary Science Letters*, *500*, 156-167.
35. Zhu, H., Li, X., Yang, J., Stern, R. J., & Lumley, D. E. Poloidal-and toroidal-mode mantle flows underneath the Cascadia Subduction Zone. *Geophysical Research Letters*, e2020GL087530.

References only in the supporting information

36. Levin, V., & Park, J. (1997). Crustal anisotropy in the Ural Mountains foredeep from teleseismic receiver functions. *Geophysical Research Letters*, *24*(11), 1283-1286.
37. Zhang, H., & Schmandt, B. (2019). Application of Ps scattering kernels to imaging the mantle transition zone with receiver functions. *Journal of Geophysical Research: Solid Earth*, *124*(1), 709-728.

Acknowledgments:

We thank K. H. Liu and S. S. Gao for sharing their SWS dataset. We also thank H. Zhu for sharing full waveform inversion results. This study is supported by NSF grants EAR-1554908 and EAR-1664471. H.Z. acknowledges support from the Caswell Silver Fellowship of the Earth and Planetary Science Department at the University of New Mexico.

Data Availability

The raw seismic data used in this study are publicly available through the IRIS Data Management Center. The receiver functions data are available at Zenodo (https://doi.org/10.5281/zenodo.3981446).

AGU PUBLICATIONS

Geophysical Research Letter

Supporting Information for

Localized anisotropy in the mantle transition zone due to flow through slab gaps

Han Zhang[1*], Brandon Schmandt[1], Jin S. Zhang[1,2]

1. Department of Earth and Planetary Science, University of New Mexico, Albuquerque, NM, USA.
2. Institute of Meteoritics, University of New Mexico, Albuquerque, NM, USA.

Contents of this file

Text S1 to S7

Figures S1 to S8

Additional Supporting Information (Files uploaded separately)

Caption for Movies S1

Text S1

The teleseismic shear wave splitting (SWS) measurements were first averaged at each station using circular averaging (Montagner et al., 2000). Then we created a $1^\circ \times 1^\circ$ grid dataset by averaging the station-based SWS measurements in a 200 km radius bin.

Text S2

The transverse energy minimization method uses a grid search framework to find the splitting parameters, fast-axis orientation and delay time, to minimize the energy of the SH component within a target time window (Long & Silver, 2009). The grid intervals for our fast-axis orientation and delay time are 1° and 0.1 s, respectively. The time windows were set as ± 4 s from the peak amplitude of the *Ps* phase on the stacked SV component. After finding the global minimum, under the assumption of Gaussian noise, it is conventional to report the uncertainty of the estimate using an F-test formulation (Walsh et al., 2013). Here we reported the 95% confidence level of our estimates.

However, given the fact that the noise may not follow a Gaussian distribution, the grid search results from low SNR phases (e.g. *P*410*s* and *P*660*s*) often suffer from an artificial global minimum unless further quality control is applied. We adopted a bootstrap based metric to qualify the reliability of the estimates based on how much they reduce the amplitude of the corrected SH stack compared to the raw SH stack (Fig. 1d). The metric was defined as

$$M = (RMS_{zero} - RMS_{min})/SD_{boot}$$

where the RMS_{zero} stands for the root-mean-square (rms) value of a zero-lag time SH stack, RMS_{min} is the rms value from the minimum energy parameters. SD_{boot} is the standard deviation of the rms values from 200 bootstrap resamples of the target SH window. A larger M means greater rms reduction and suggests a more reliable global minimum. Examples with various M values can be found in Fig. S5. Figure. 1d only gives the estimates from the *P*660*s* phase with M greater than 3.

Text S3

Since the *P*410*s* and *P*660*s* phases are much weaker than the *SKS* phase, stacking receiver functions from different azimuths is required to obtain stable measurements. Synthetic tests indicate that the polarity of the *Ps* phases on the SH component changes when the back azimuth crosses the fast- or slow-axis of anisotropy (Fig. S6). Therefore, to prevent deconstructive interference of traces from different azimuths during stacking, we flipped the SH traces in the 2nd and 4th quadrants using the fast-axis orientation estimated from the *P*660*s* phase. The flip was applied to both *Ps* phases because the null hypothesis of an isotropic mantle transition zone (MTZ) suggests that the two *Ps* phases share the same fast-axis orientation.

The amplitude ratio was then measured as the peak shear wave amplitude on the integrated stacked SH component over that on the stacked SV component (hereinafter referred to as P_{SH}/P_{SV}). Theoretically, under weak anisotropy (delay time less than a tenth of a period), the P_{SH}/P_{SV} amplitude ratio is proportional to the delay time (Montagner et al., 2000). Synthetic tests demonstrate that the positive correlation continues to moderate anisotropy (delay time up to one third of a period), where the amplitude ratio becomes increasingly sensitive as the magnitude of anisotropy increases (Fig. S1).

Bootstrap resampling, with 200 samples, was used to assess the uncertainties of the amplitude ratios assuming a normal distribution of the resampled stacks. The paired Cohen's distance was calculated using the following equation

$$Cohen's\ d = (\overline{AmpR_{660}} - \overline{AmpR_{410}})/SD_{diff}$$

where $\overline{AmpR}$ is the mean of measured amplitude ratios for the *P*410*s* and *P*660*s* phase, and SD_{diff} is the standard deviation of the two groups' difference. Using the corresponding paired 2-sample t-test, a two-tailed 68% confidence level would require Cohen's distance either greater than 1.0 or smaller than -1.0. A two-tailed 95% confidence level sets thresholds at ±2.0. The observed Cohen's distances were superimposed on the tomographic map in Figure. 2b.

Text S4

We explored the effects of two anisotropic layers with different fast-axis orientations using synthetic data (Fig. S3; Supporting Information S7). The anisotropy in the top layer (36 - 320 km) is 2.5%, and that of the bottom layer (360 - 556 km) is 1.5%. Accordingly, the delay times from the two layers are ~1.3 s and ~0.5 s respectively. The fast-axis orientation of the upper layer was fixed at 89˚, which is the mean fast-axis orientation estimated from the *P*660*s* phase (Fig. S6).

Since the top layer dominates the depth-integrated anisotropic effect, the fast-axis orientation estimations from the energy minimization method show no significant difference with the 95% confidence intervals. Such results suggest the fast-axis orientation measurements are not ideal to constrain differential orientations if the common layer dominates the total anisotropic effect. In contrast, the delay times show greater variations with respect to the differential orientations, but are still less sensitive when compared with the Cohen's distances.

Increasing the differential orientation between the two layers moves the resulting Cohen's distances from a constructive interference area (0˚ - 30˚) to a neutral area (40˚ - 60˚), and finally to a destructive interference area (70˚ - 90˚). Such results provide an alternative fit to the neutral observations and a potential explanation for the deconstructive observations in Fig. 2b.

Text S5

To illustrate a range of possible anisotropic structures beneath our study region, we constructed three types of forward seismic models in Fig. 3a. Several constraints were taken from the previous seismic model, mineral physics data, and our observation here from *P*660*s*. Firstly, the depths of mantle discontinuities come from previous migration results (Zhang & Schmandt, 2019). The depth-integrated delay time from the three models were set to match the mean estimated delay time from the *P*660*s* in the best resolved regions (light background in Fig. 1d), which is 1.4 s (Fig. S7). Such a setting makes the three models indistinguishable from *SKS* data alone.

Moreover, from bottom to top, we listed the detailed constraints in each layer below.

Lower mantle

- The agreement between the splitting parameters from the *P*660*s* and SWS suggests an isotropic lower mantle (Fig. 1d), which applies to all three models.

Mantle transition zone

1. As a control group, there is no transition zone anisotropy in model #1.
2. At the ambient mantle, mineral physics data suggested a nearly isotropic lower transition zone layer even lattice preferred orientation of ringwoodite was developed (Fig. S4). Therefore, model #2 has an isotropic lower MTZ layer. We further assumed a uniform upper MTZ layer with gradual transition at the 520 for simplicity.

3. When slab is present in the transition zone, atypical minerals such as phase E and akimotoite may contribute to the recorded anisotropic signal. Therefore, the deeper anisotropic layer in model #3 is set to match the depth extent (~380 km to ~620 km) of the slab suggested from tomographic results (Fig. 2c).

At the 410

1. As a control group, there is no anisotropy near the 410 in model #1.
2. At the ambient mantle, mineral physics data suggested a ~30% anisotropy drop across the 410 in a pyrolite model, which comes from the lower intrinsic elastic anisotropy of wadsleyite compared with olivine (Fig. S4). Under the assumption of simple shear deformation from mantle flow, the ~30% drop was honored in model #2.
3. When slab is present in the transition zone, the deformation may not follow the simple shear assumption. Therefore, we didn't implement any constraints at the 410 in model #3.

Upper mantle

- Surface wave studies in this region suggest ~1-2% azimuthal anisotropy within the first ~200 km (Wagner & Long, 2013), which applies to all three models. Due to the poor depth resolution in the upper mantle of our data, and for the sake of simplicity, we further assumed a uniform anisotropy strength in the upper mantle layer for all three models.

Crust

- There is no clear evidence of strong crustal anisotropy so we set it to be zero for simplicity.

While there are countless models that are consistent with the observational constraints, depth resolution is inadequate to constrain detailed structure. So, we consider three models to highlight potential anisotropy contributions from the upper mantle above 410 km, the upper transition zone where wadsleyite is stable, and the lower transition zone. The detailed parameters of our models are listed below.

1. Model #1 only contains an anisotropic layer extending from the Moho (at 36 km) to 400 km. The strength of anisotropy is 2.0% from the Moho down to 320 km and then linearly decreases to 0% at 400 km. The 80 km gradual

transition avoids strong artificial P-to-S conversions on the synthetics, which were not found in observational receiver functions.

2. Model #2 has a uniform anisotropic layer from the Moho down to the 410 discontinuity (at 428 km), which is underlain by another uniform layer of anisotropy in the upper MTZ (428-556 km). The strength of anisotropy in the upper mantle layer is 1.4% and that of the upper MTZ layer is 1.0%. The ~30% drop in the strength across the 410 discontinuity comes from the mineral physics constraints mentioned before. A 40 km thick 520 discontinuity (at 556 km) was set to avoid strong artifacts.
3. Model #3 has two separated anisotropic layers. The top layer (Moho-260 km) has a strength of 1.0% while the deeper one (380-620 km) has a maximum strength of 3.0%. To avoid artifacts from sharp contrast, the lower boundary of the top layer and the two boundaries of the second layer have gradual transitions over 80 km.

Using synthetic receiver functions (Supporting Information S7), figure 3a and S7 give the distribution of the amplitude ratios and the estimated splitting parameters from the three models.

Text S6

We used a grid search method to invert preferred models for explaining the observed amplitude ratios. At each stacking point, we used noise-free synthetics with a ray parameter and back-azimuth distribution identical to the observation. Such a process ensures the magnitudes of anisotropy within the two layers are the only factors affecting the amplitude ratios.

In the model #2 parameterization, the top layer has a uniform anisotropy between the Moho and 320 km depth. The second layer starts from 400 km and extends down to 556 km. The 30% anisotropy drop across the 410 (at 428 km) is kept in the second layer. From 320 km to 400 km, a gradual transition between the two layers was applied to avoid strong artifacts. The two magnitudes used in the grid search are the uniform anisotropy in the top layer and the maximum anisotropy in the upper transition zone layer (Fig. 3a, #2).

In the model #3 parameterization, the top layer extends from the Moho to 260 km. The second layer starts at 380 km and extends to 620 km. Gradual transitions over 80 km at the boundaries are applied. The two magnitudes in grid search are the maximum anisotropy within the two layers (Fig. 3a, #3).

The P_{SH}/P_{SV} of the $P410s$ and $P660s$ phases from each of the models were calculated using noise-free synthetics. The two standardized squared deviations from the observed means were summarized as a misfit term.

$$Q = (\Delta AmpR_{410}/SD_{410})^2 + (\Delta AmpR_{660}/SD_{660})^2$$

where $\Delta AmpR$ is the difference between observed and predicted amplitude ratios for the $P410s$ and $P660s$. SD is the standard deviation of observed amplitude ratios. Given the assumption of normally distributed amplitude ratios, the misfit term Q approximately follows a chi-square distribution with a 2 degrees of freedom (Fig. S8). Accordingly, the 68% confidence intervals of our best fit model were reported using the chi-square distribution in Fig. 3b and c.

When interpreting the inverted magnitudes of anisotropy in the upper mantle and transition zone layers, please keep in mind that only the depth-integrated anisotropy in each layer is constrained rather than the magnitude of anisotropy at a specific depth. Consequently, there is a tradeoff between the strength and thickness of anisotropy within either the upper mantle or transition zone. The upper mantle layer is thicker, so the potential tradeoff is larger. For instance, if anisotropy were concentrated in only a 100 km depth interval of the upper mantle (e.g., mantle lithosphere or asthenosphere), then the actual magnitude of anisotropy would be locally greater than our estimates. The tradeoff may span a smaller range of values in the transition zone layer because it is thinner. For a pyrolite composition, almost all anisotropy is expected in the wadsleyite stability field from about 410 to 520 km (Fig. S4). We consider it less likely that only a subset of the wadsleyite depth interval contains anisotropy because it is smaller and does not include major rheological contrasts. Thus, the optimized values for the transition zone layer are a more localized constraint on the actual magnitude of anisotropy (Fig. 3b and c).

Text S7

The synthetic receiver functions were generated using a reflectivity method (Levin & Park, 1997). Identical to the processes applied on the observed data, the synthetic receiver functions were rotated to the P-SV-SH coordinate and were filtered between 0.07 Hz and 0.25 Hz. We then contaminated the synthetics with pre-event noise collected from observed USArray data. We assumed a P wave SNR of 5 when adding the noise to the synthetics. Normal moveout correction was applied to the synthetics using the input velocity model. Using a ray parameter and back-azimuth distribution identical to the whole PNW dataset, the noisy synthetics produce the forward modeling results in Fig. 3a, Fig. S3 and Fig. S7.

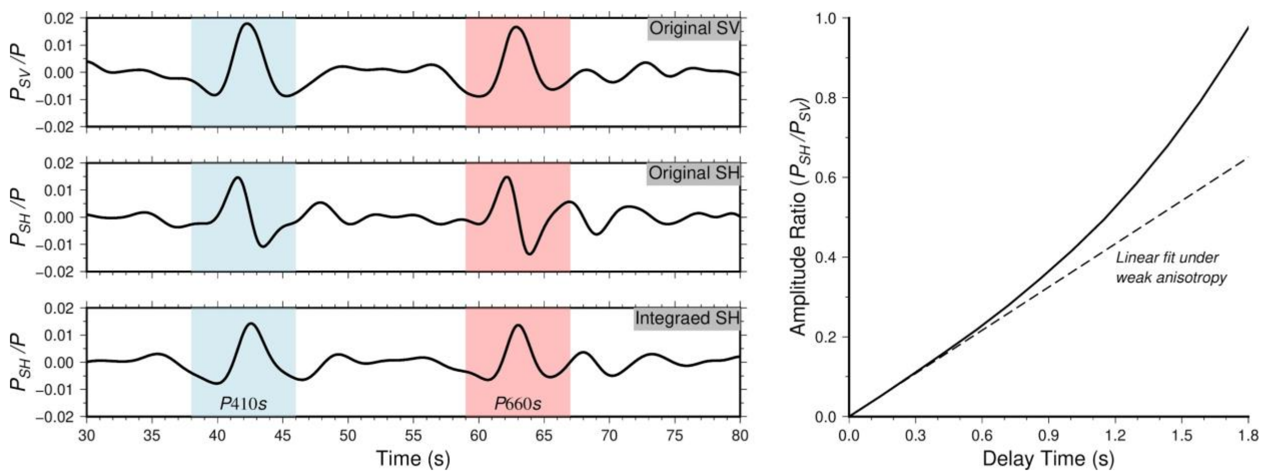

Fig. S1. Synthetic receiver function from an anisotropic upper mantle model and the relationship between the P_{SH}/P_{SV} amplitude ratios and delay times. The amplitude ratio P_{SH}/P_{SV} is measured as the peak shear wave amplitude on the integrated SH component over that on the original SV component. The amplitude ratios are approximately proportional to the delay times under weak anisotropy. At moderate anisotropy, the amplitude ratios become increasingly sensitive to the magnitude of anisotropy.

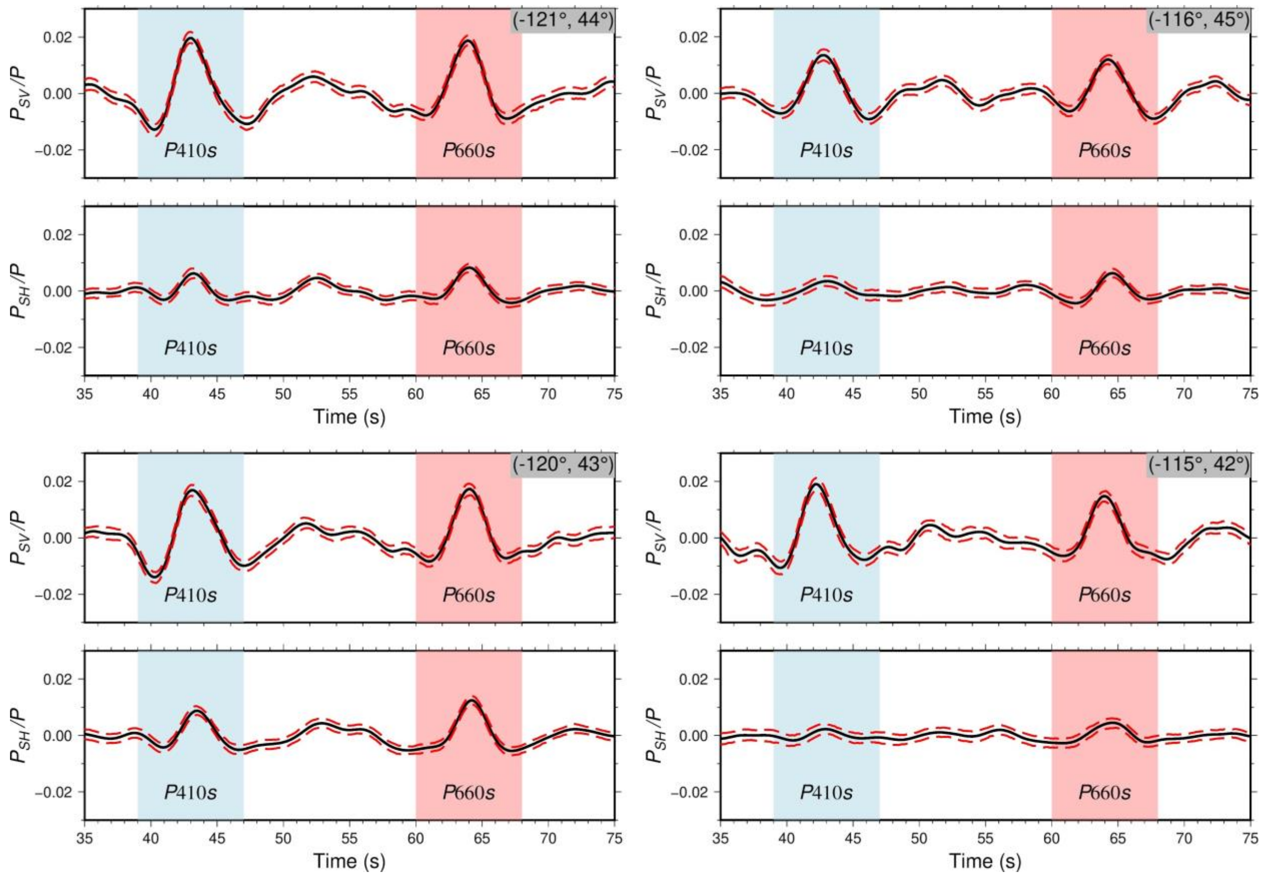

Fig. S2. Additional receiver function examples that require mantle transition zone anisotropy. The locations are labeled at the top right corner. The red dashed line represents the 95% confidence level of the stacked traces from bootstrap resampling.

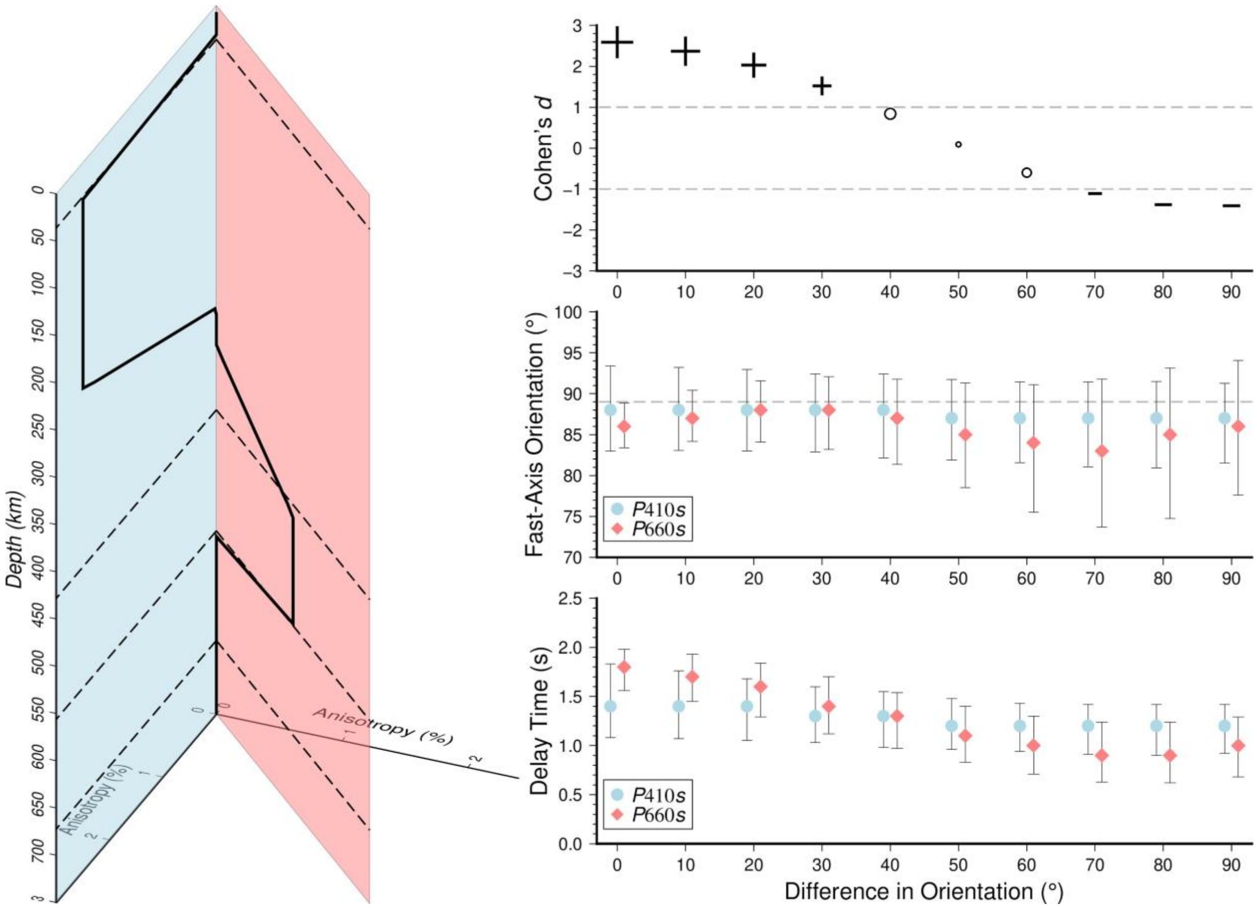

Fig. S3. Synthetic results of two anisotropic layers with different orientations. Cohen's distance shows the greatest sensitivity to the variation of differential orientations among the three measurements.

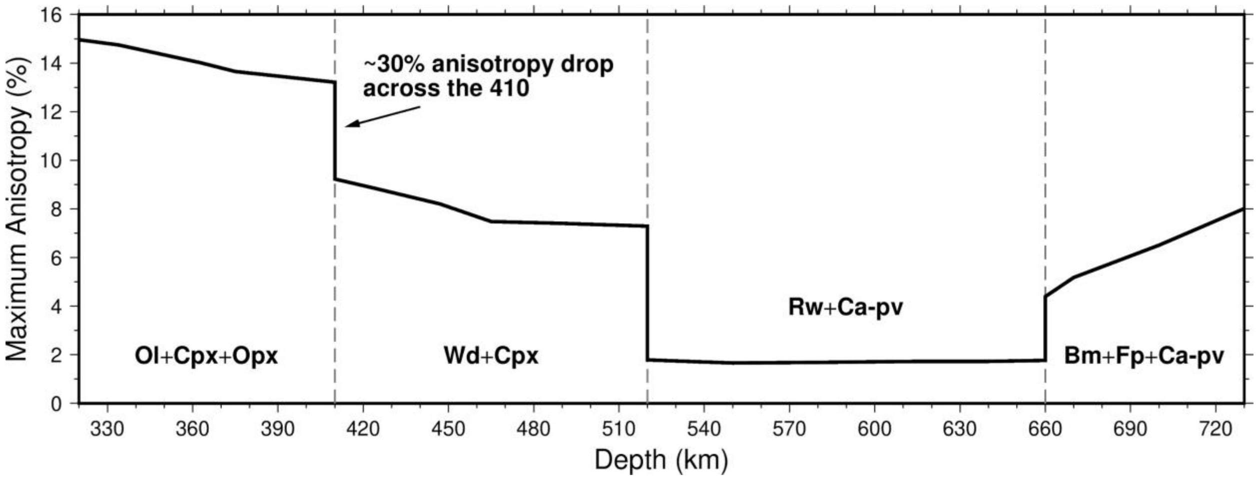

Fig. S4. Maximum shear wave anisotropy indicated from a pyrolite model. There is an ~30% anisotropy drop across the 410 discontinuity primarily due to the significantly lower intrinsic anisotropy of wadsleyite compared with olivine. Only the minerals contributing to the calculated anisotropy are labeled in the figure: olivine (Ol), clinopyroxene (Cpx), orthopyroxene (Opx), wadsleyite (Wd), ringwoodite (Rw), Ca-perovskite (Ca-pv), bridgmanite (Bm), ferropericlase (Fp).

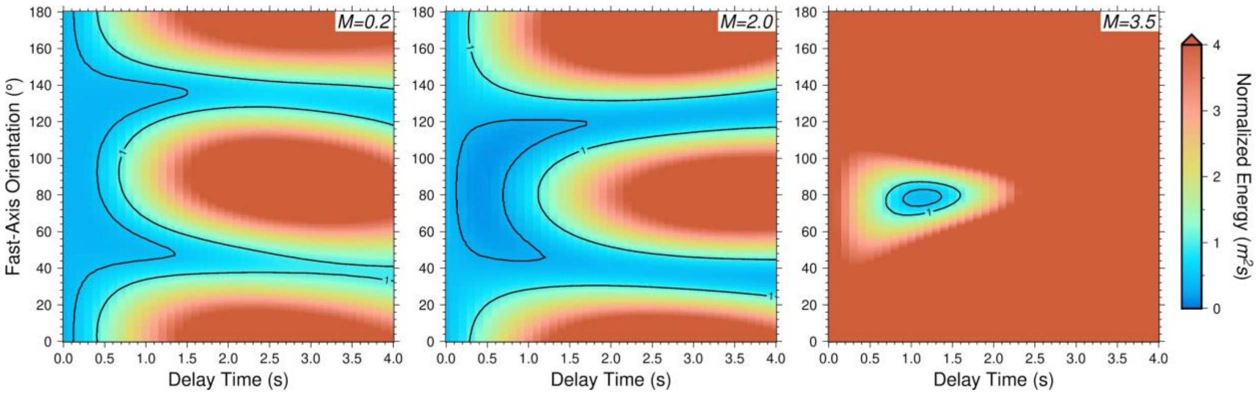

Fig. S5. Examples of the energy minimization results with various *M* values. The *M* values are labeled at the top right corner. The contoured line with normalized energy equal to 1 represents the 95% confidence interval from the F-test. The inner contour represents the 68% confidence interval.

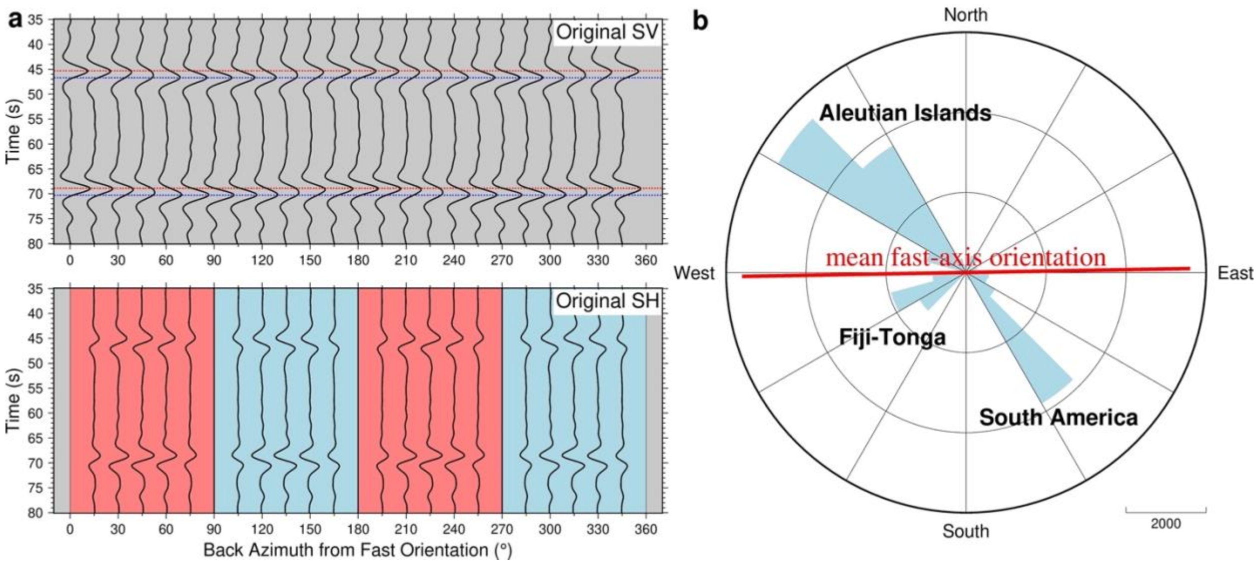

Fig. S6. Synthetic receiver functions and back azimuth distribution of the PNW dataset. (**a**) The top panel shows synthetic receiver functions on the SV component while the bottom panel shows the SH components. The SH components flip polarity after the back-azimuth crosses the fast- or slow-axis. (**b**) The mean fast-axis orientation (89˚) estimated from the *P*660*s* phase is shown by the red solid line. Three regions (Aleutian Islands, South America, and Fiji-Tonga) contributed the majority of the receiver functions in this study.

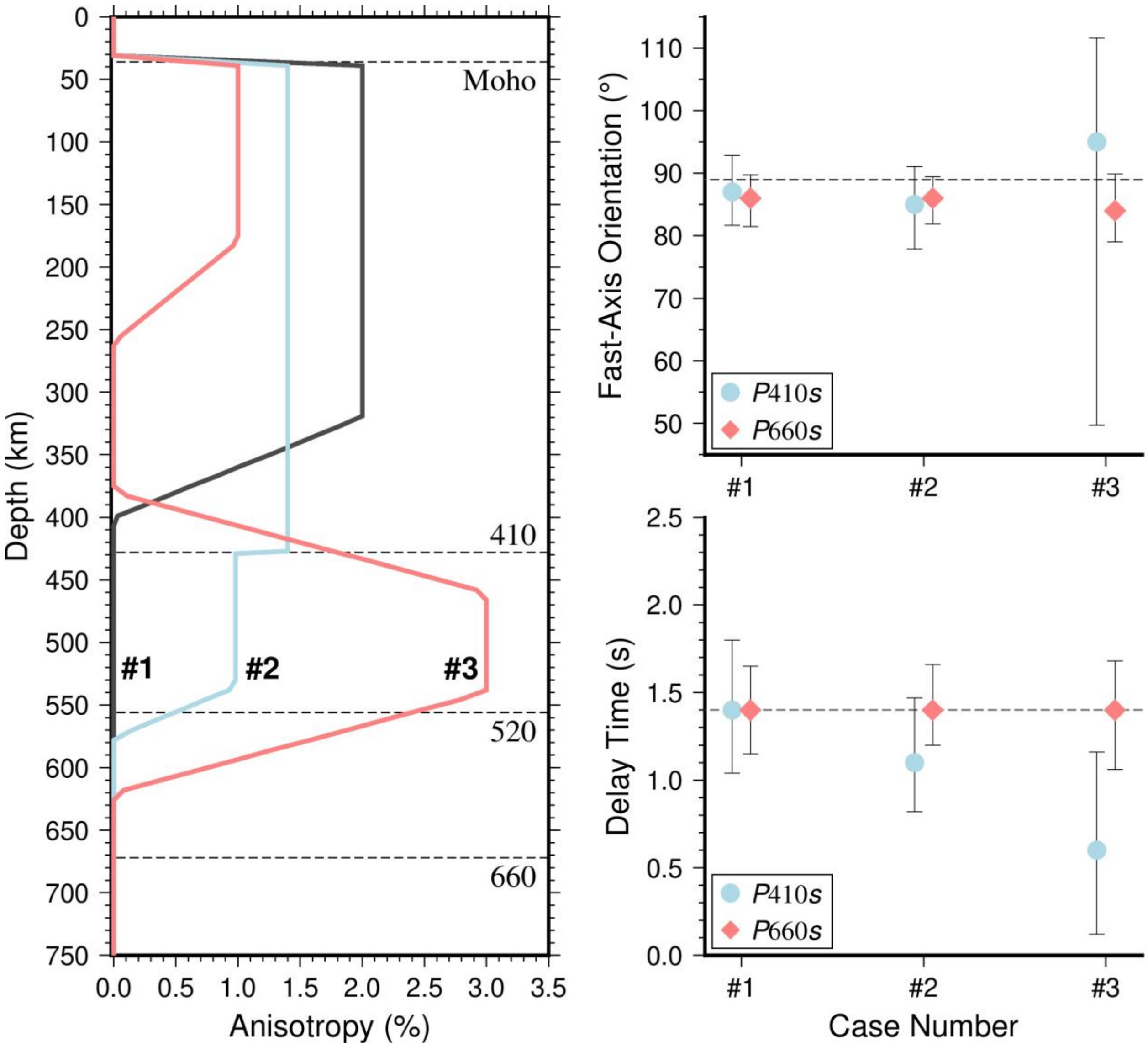

Fig. S7. Forward models and splitting estimations from energy minimization method. All three input models have a fast-axis orientation of 89˚ and a delay time from *P*660*s* of ~1.4 s. The energy minimization method successfully recovers the input with the 95% confidence intervals.

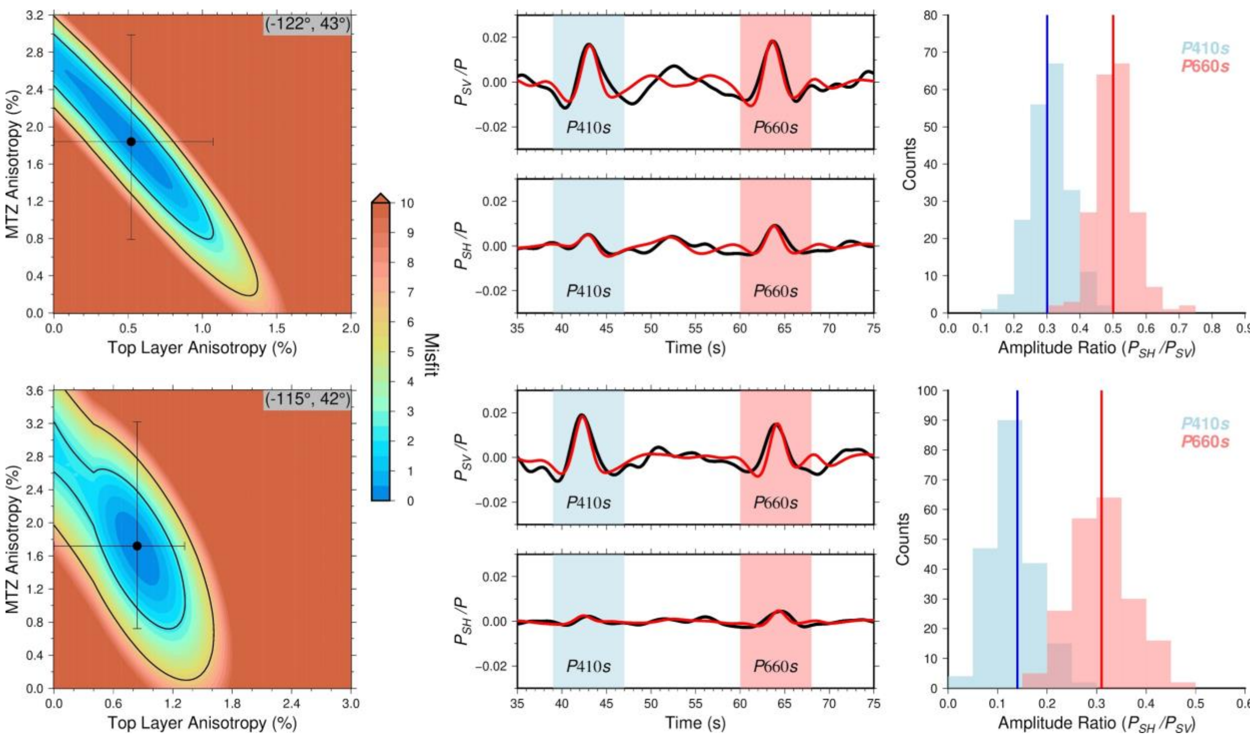

Fig. S8. Examples of misfit distribution from grid search inversion and best fit model. The left panel shows the distribution of the misfit Q. The locations are labeled at the top right corner. The two black contour lines denote the 68% and 95% confidence interval of the estimated parameters respectively. We represented the intervals in Fig. 3b and c using the error bar boxing the 68% area. The middle panel gives the observed receiver functions (black) and the synthetic waveforms (red) from the best fit model. The right panel shows the observed amplitude ratio distributions and the predictions from the best fit model (vertical lines).

Movie. S1. Isosurface of 1% high P wave velocity anomalies beneath the PNW. The locations showing significant anisotropy are denoted by solid spheres at 500 km depth. The white ones indicate constructive interference while the black ones represent deconstructive interference.